JACS
JOURNAL OF THE AMERICAN CHEMICAL SOCIETY

Article

pubs.acs.org/JACS

Redox Potentials of Colloidal n-Type ZnO Nanocrystals: Effects of Confinement, Electron Density, and Fermi-Level Pinning by Aldehyde Hydrogenation

Gerard M. Carroll, Alina M. Schimpf, Emily Y. Tsui, and Daniel R. Gamelin*

Department of Chemistry, University of Washington, Seattle, Washington 98195-1700, United States

Supporting Information

ABSTRACT: Electronically doped colloidal semiconductor nanocrystals offer valuable opportunities to probe the new physical and chemical properties imparted by their excess charge carriers. Photodoping is a powerful approach to introducing and controlling free carrier densities within free-standing colloidal semiconductor nanocrystals. Photoreduced (n-type) colloidal ZnO nanocrystals possessing delocalized conduction-band (CB) electrons can be formed by photochemical oxidation of EtOH. Previous studies of this chemistry have demonstrated photochemical electron accumulation, in some cases reaching as many as >100 electrons per ZnO nanocrystal, but in every case examined to date this chemistry maximizes at a well-defined average electron density of $\langle N_{max} \rangle \approx (1.4 \pm 0.4) \times 10^{20}$ cm^{-3}. The origins of this maximum have never been identified. Here, we use a solvated redox indicator for *in situ* determination of reduced ZnO nanocrystal redox potentials. The Fermi levels of various photodoped ZnO nanocrystals possessing on average just one excess CB electron show quantum-confinement effects, as expected, but are >600 meV lower than those of the same ZnO nanocrystals reduced chemically using Cp*$_2$Co, reflecting important differences between their charge-compensating cations. Upon photochemical electron accumulation, the Fermi levels become independent of nanocrystal volume at $\langle N \rangle$ above ~2×10^{19} cm^{-3}, and maximize at $\langle N_{max} \rangle \approx (1.6 \pm 0.3) \times 10^{20}$ cm^{-3}. This maximum is proposed to arise from Fermi-level pinning by the two-electron/two-proton hydrogenation of acetaldehyde, which reverses the EtOH photooxidation reaction.

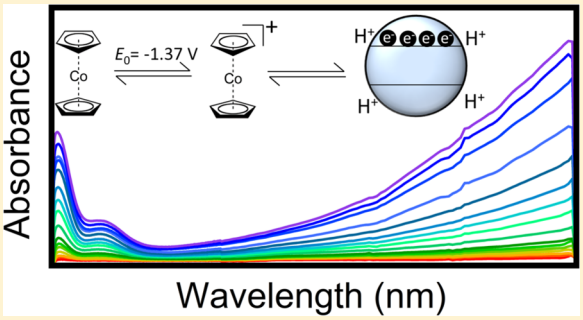

INTRODUCTION

Photodoping offers a convenient method for tuning carrier densities in colloidal semiconductor nanocrystals. Photochemical n-doping to yield excess delocalized band-like electrons has been studied for a variety of colloidal nanocrystals, including ZnO,[1−6] In_2O_3,[7] and CdE (E = S, Se, Te),[8] and with a variety of hole quenchers.[6] The most thoroughly investigated system has been colloidal ZnO nanocrystals reduced using ethanol (EtOH) as the hole quencher.[1,3−6] Upon nanocrystal photoexcitation, an electron is excited from the valence band (VB) to the conduction band (CB). The photogenerated hole is then quenched within picoseconds,[9] leaving the electron in the ZnO CB. EtOH oxidation liberates protons (H^+) that compensate the CB electron charges, with acetaldehyde as the two-electron/two-proton oxidation product[10,11] according to the stoichiometry of eq 1.

$$ZnO + 1/2CH_3CH_2OH \xrightarrow{h\nu} e^-_{CB}{:}ZnO{-}H^+ + 1/2CH_3CHO \quad (1)$$

In this system, multiple delocalized CB electrons per ZnO nanocrystal can be accumulated photochemically, with the average ($\langle n \rangle$) reaching as high as >100 in some cases.[6] Under rigorously anaerobic conditions, the CB electrons are stable after terminating the nanocrystal photoexcitation,[5] making these n-doped ZnO nanocrystals well suited for further spectroscopic or chemical investigations. The average maximum number of electrons per nanocrystal ($\langle n_{max} \rangle$) was found to be proportional to nanocrystal volume, such that the average maximum electron *density* is constant for all sizes at $\langle N_{max} \rangle \approx 1.4 \times 10^{20}$ cm^{-3} for ZnO photodoped using EtOH.[6] The microscopic origin of this maximum remains unidentified, and both kinetic and thermodynamic limitations to further electron accumulation can be postulated.[2,6]

Photoluminescence measurements[12,13] and electron-transfer chemistries[14,15] provide strong evidence that the potentials of CB electrons in colloidal ZnO nanocrystals are subject to quantum confinement effects, but these measurements have only probed the limit of $\langle n \rangle = 1$. The ability to accumulate tens to hundreds of excess CB electrons per nanocrystal via photodoping raises intriguing questions about how to describe the redox potentials and Fermi levels (E_F) of such heavily reduced ZnO nanocrystals, and the dependence of these parameters on the method of reduction.

Received: June 29, 2015
Published: August 11, 2015

DOI: 10.1021/jacs.5b06715
J. Am. Chem. Soc. 2015, 137, 11163−11169

Here, we report contactless *in situ* determination of the redox potentials of n-type colloidal ZnO nanocrystals using an optical redox indicator. The data show that E_F is subject to quantum confinement effects in the limit of one electron per nanocrystal, as anticipated from prior results. With further electron accumulation, however, E_F becomes independent of quantum confinement and depends only on electron density. E_F is shown to depend strongly on the identity of the charge-compensating cation, spanning a range of ~600 meV when only one electron per nanocrystal is present, consistent with previous reactivity studies.[16] $\langle N_{max} \rangle$ and E_F^{max} are found to be determined by electron Fermi-level pinning, which occurs at the same potential for all nanocrystal sizes. Aldehyde hydrogenation, i.e., the two-electron/two-proton reaction that reverses the EtOH photo-oxidation, is proposed to be the microscopic origin of this Fermi-level pinning.

METHODS

ZnO Nanocrystal Synthesis. Colloidal ZnO nanocrystals were synthesized by base-initiated hydrolysis and condensation of Zn^{2+} as detailed previously.[17,18] In a typical synthesis, a solution of 22 mmol of tetramethylammonium hydroxide in 40 mL of EtOH was added dropwise to a stirred solution of 13 mmol of $Zn(OAc)_2$ in 135 mL of dimethyl sulfoxide at room temperature. Nanocrystals were grown for ~1 h, after which the reaction was stopped by precipitation with 300 mL of ethyl acetate. Nanocrystals were collected via centrifugation and resuspended in EtOH, followed by precipitation with heptane. To suspend the nanocrystals in nonpolar solvents, the surface ligands were exchanged by suspending the nanocrystals in excess of dodecylamine (DDA) that had been heated above the melting point (29 °C), followed by precipitation with EtOH. Finally, the nanocrystals were heated in trioctylphosphine oxide (TOPO, 90%) at 130 °C for 30 min. The resulting TOPO-capped nanocrystals were then washed with 3:1 EtOH/toluene and resuspended in toluene. The largest ZnO nanocrystals were made in a similar manner but were heated under N_2 in DDA at 180 °C for ~24 h prior to TOPO capping to promote growth to various sizes.

Physical Characterization. UV−vis−NIR absorption spectra were collected in a 1 cm air-free quartz cuvette using a Cary 500 spectrometer, with typical nanocrystal concentrations of 5−20 μM. The radii of small nanocrystals ($r \leq 2.8$ nm) were determined from the empirical correlation between radii and absorption spectra.[13,19] The radii of larger nanocrystals ($r = 3.7$ nm) were determined by statistical analysis of transmission electron microscopy (TEM) images collected using a FEI Tecnai G2 F20 instrument. ZnO nanocrystal concentrations were determined analytically. First, 200 μL of the nanocrystal suspension was dried and digested in 200 μL of ultrapure nitric acid (TraceSELECT, Fluka). The resulting solution was diluted with a known amount of ultrapure water (10.00 g, measured to two decimal places on a balance), and the Zn^{2+} concentration was measured using inductively coupled plasma atomic emission spectroscopy (PerkinElmer 8300 instrument). The nanocrystal concentration was then calculated using the known dilution factors and nanocrystal radii to convert from Zn^{2+} concentration to nanocrystal concentration.

Photodoping. ZnO nanocrystals were suspended in dry, anaerobic toluene/tetrahydrofuran (THF) (1:14) solutions and prepared in a 1 cm air-free cuvette, and then photodoped to their maximum level by prolonged exposure to UV irradiation from a 100 W Hg/Xe Oriel broad-band photolysis lamp (2 W/cm^2, 1.5 cm illumination diameter) in the presence of EtOH and $[Cp_2Co][PF_6]$ (0.233−0.633 mM). THF was used to aid the solubility of $[Cp_2Co][PF_6]$. The UV−vis−NIR absorption was collected periodically during the photodoping process. When the NIR absorption did not change over 20 min of UV exposure, the nanocrystals were considered to have reached their maximum photodoping level. Maximum photodoping was typically achieved within 90 min of UV irradiation.

Electron Counting by Titration. The average number of photodoped electrons per ZnO nanocrystal ($\langle n \rangle$) was determined by titration with $[FeCp^*_2][BAr_F]$ (Figure S1).[6,20,21] Aliquots of $[FeCp^*_2][BAr_F]$ in THF were added to the maximally photodoped nanocrystals, and the reduction of the NIR absorption was monitored. After complete elimination of the NIR absorption, additional aliquots led to growth of $FeCp^*_2$ absorption centered at 700 nm. The data were then fit with a linear function, and the maximum number of photodoped electrons was determined from the x-intercept of the fitted line.

Electron Counting from NIR Absorption. The average number of electrons per nanocrystal, $\langle n \rangle$, was determined spectroscopically from the NIR absorption involving intra-band transitions of the CB electrons. For this, molar extinction coefficients (ε) were determined for each ZnO nanocrystal size at five different wavelengths (500, 778, 1000, 1300, and 1600 nm) and at various values of $\langle n \rangle$, by $[FeCp^*_2][BAr_F]$ titration. These ε values were fit to a power function with the general form $\varepsilon_\lambda = Q_\lambda \langle n \rangle^p$ (Figure S1b), where Q (M^{-1} cm^{-1} $electron^{-1}$) and p (unitless) are constants. Substituting into the Beer's law equation and rearranging for $\langle n \rangle$, the expression becomes $\langle n \rangle = Abs_\lambda \exp(p)/Q_\lambda bC$, where b is the optical path length (cm) and C is the concentration (M). Values of $\langle n \rangle$ calculated from the absorption at 778, 1000, 1300, and 1600 nm were averaged together to obtain the reported values of $\langle n \rangle$, with error bars reported as $\pm \sigma$ from the mean value of $\langle n \rangle$. The $\langle n \rangle$ values reported here were measured without UV illumination. Under these conditions, $\langle n \rangle$ is constant.

Optical Fermi-Level Measurements. Fermi levels (E_F) were measured using Cp_2Co as an *in situ* optical redox indicator. Measurements of E_F were performed in the absence of UV photoexcitation. Under these conditions, $\langle n \rangle$ and E_F are stable. Cp_2Co concentrations were measured spectroscopically using the absorption feature at 500 nm ($\varepsilon_{500} = 301$ M^{-1} cm^{-1}),[22] accounting for overlapping ZnO intra-band absorption. Cp_2Co concentrations were then determined using Beer's law, and E_F was calculated from the Nernst equation. The E_F values reported here are thus equilibrium values measured without UV illumination and are stable under rigorously anaerobic conditions.

RESULTS AND ANALYSIS

Figure 1A plots electronic absorption spectra of colloidal ZnO nanocrystals ($r = 1.9$ nm) collected at various stages of nanocrystal photodoping using EtOH as the hole quencher. In these measurements, $[Cp_2Co][PF_6]$ (Cp_2Co^+ = cobaltocenium, PF_6^- = hexafluorophosphate) has been added to the reaction mixture for use as an optical redox indicator. As detailed previously, photodoping leads to bleaching of the ZnO band-edge absorption (inset) and growth of a comparably intense IR intra-band absorption feature, both indicating a growing population of delocalized CB electrons (e^-_{CB}).[1−3,5,6,14−16,23−26] The IR absorbance can be analyzed to provide the average number of electrons per ZnO nanocrystal ($\langle n \rangle$) at each level of photodoping. In the present experiments, new absorption features at 390 and 500 nm are also observed upon photodoping, attributable to the LMCT and d−d transitions of cobaltocene (Cp_2Co), respectively.[22] The concentration of Cp_2Co is determined from the Cp_2Co absorbance at 500 nm and its extinction coefficient ($\varepsilon_{500} = 301$ M^{-1} cm^{-1}) using Beer's law. Using the Nernst equation (eq 2)

$$E_F\ (V) = E_{cell}\ (V) = E^\circ - 0.02568 \ln \frac{[Cp_2Co]}{[Cp_2Co^+]} \qquad (2)$$

and the experimental Cp_2Co redox potential ($E^\circ = -1.37$ V vs Fc^+/Fc, see Supporting Information), the solution potential (E_{cell}) may then be calculated. As measured by the quotient $[Cp_2Co]/[Cp_2Co^+]$, E_{cell} directly reports the electron Fermi level (E_F) of the ensemble of ZnO nanocrystals,[27,28] which are in thermodynamic equilibrium with the Cp_2Co^+/Cp_2Co couple.

DOI: 10.1021/jacs.5b06715
J. Am. Chem. Soc. 2015, 137, 11163−11169

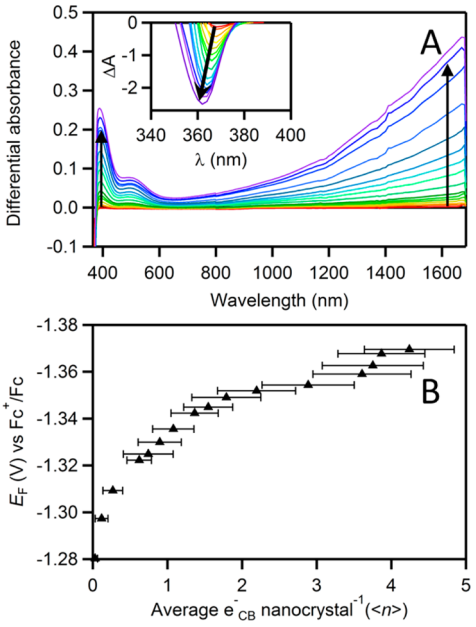

Figure 1. (A) Representative differential electronic absorption spectra collected at various illumination times between 0 and 1 h during photochemical reduction of 9.45 μM colloidal ZnO (r = 1.9 nm) nanocrystals in the presence of 466 μM $[Cp_2Co][PF_6]$ in a 14:1:0.5 THF/toluene/EtOH mixture. The main panel shows the visible spectral range, and the inset shows the UV (ZnO inter-band) range. Note the different y-axis scaling. The arrows indicate the direction of increased photodoping. (B) Plot of electron Fermi level (E_F, ▲) vs average number of CB electrons per nanocrystal ($\langle n \rangle$), calculated from the Cp_2Co absorbance at λ = 500 nm (ε_{500} = 301 $M^{-1}cm^{-1}$) at each stage of photodoping. E_F values are referenced to the ferrocenium/ferrocene (Fc^+/Fc) redox couple. The error bars indicate $\pm\sigma$ from the mean value of $\langle n \rangle$. The quotient $[Cp_2Co]/([Cp_2Co] + [Cp_2Co^+])$ is ~0.5 at $\langle n_{max} \rangle$ in these measurements.

The solution potential therefore equals the ZnO electron Fermi level.

Figure 1B plots E_F vs $\langle n \rangle$ for the entire data set of Figure 1A. Initially, mixing undoped ZnO nanocrystals with Cp_2Co^+ yields no detectable Cp_2Co, indicating that E_F of the undoped ZnO nanocrystals is far more positive than −1.37 V (the Cp_2Co^+/Cp_2Co redox couple). Upon UV photoexcitation of this mixture, E_F increases rapidly in concert with ZnO photodoping, growing from −1.28 to ~ −1.35 V, where its value levels off until $\langle n \rangle \approx$ 3.7, at which point E_F increases sharply to reach its maximum value of $E_F^{max} \approx -1.37$ V at $\langle n \rangle$ = 4.3. This value of $\langle n \rangle$ is the maximum number of electrons ($\langle n_{max} \rangle$) that can be introduced under these conditions.[6] Further UV irradition yields no change in $\langle n \rangle$ or E_F. The full range of E_F in these data is ~90 meV, smaller than the ~350 meV range measured in electrochemical ZnO nanocrystal reduction experiments.[29] This difference is in large part due to the absence of an E_F data point prior to photodoping, and it may also relate to the different counterions of the two measurements (*vide infra*).

Measurements under the same photodoping conditions but using different Cp_2Co^+ concentrations all yield the same values of E_F vs $\langle n \rangle$ (see Supporting Information). Additionally, when the weaker oxidant decamethylcobaltocenium ($Cp^*_2Co^+$, E° = −1.91 V vs Fc/Fc^+ in MeCN[30]) is added instead of Cp_2Co^+, no formation of decamethylcobaltocene (Cp^*_2Co) is observed (see Supporting Information). Together, these results confirm that the Cp_2Co^+/Cp_2Co redox couple is indeed in equilibrium with the ZnO nanocrystals.

We have previously reported that $\langle n_{max} \rangle$ in photodoped ZnO nanocrystals scales with nanocrystal volume,[6] but the fundamental origins of this scaling have not been identified. It is possible that $\langle n \rangle$ is limited kinetically, for example by the lifetimes of photogenerated holes, but it is also possible that $\langle n \rangle$ is limited thermodynamically, for example by reductive metallization of the ZnO nanocrystals at high carrier densities.[6] To address this issue, we have used this redox-indicator method to measure changes in E_F with changes in $\langle n \rangle$ for ZnO nanocrystals of three different sizes, and the results are summarized in Figure 2. From Figure 2A, the largest ZnO nanocrystals (r = 3.7 nm)

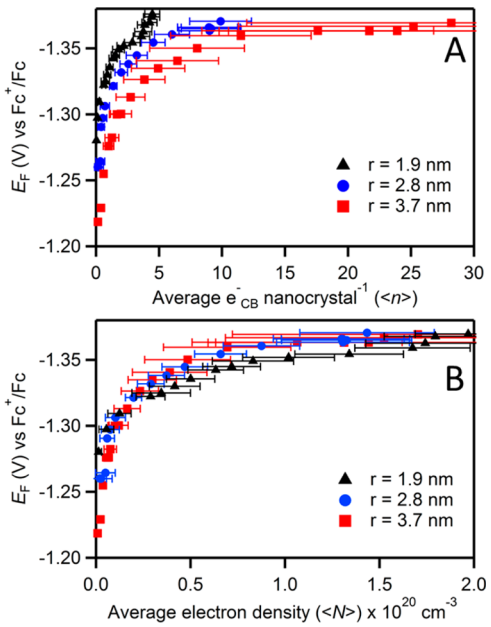

Figure 2. (A) E_F values for r = 1.9 nm (5 μM, black triangles), 2.8 nm (8 μM, blue circles), and 3.7 nm (6 μM, red squares) ZnO nanocrystals photodoped with EtOH, plotted vs $\langle n \rangle$. (B) The same E_F data plotted vs average electron density ($\langle N \rangle$). E_F values are referenced to the ferrocenium/ferrocene (Fc^+/Fc) redox couple.

show the least negative E_F value at $\langle n \rangle$ = 1, followed by the intermediate (r = 2.8 nm) and then the smallest (r = 1.9 nm) nanocrystals. From the optical bandgap energies of this series of nanocrystals (see Supporting Information) and the optically deduced ratio of CB-to-bandgap shifts with quantum confinement,[12,15] the CB energy is predicted to shift negatively by ~76 meV on going from r = 3.7 to 1.9 nm. In good agreement with this prediction, the data in Figure 2A show a shift of ~60 meV at $\langle n \rangle$ = 1, the two values being indistinguishable within the uncertainty in $\langle n \rangle$ ($\sigma = \pm 0.2$ electron at $\langle n \rangle$ = 1). The effect of quantum confinement on E_F in the one-electron limit is thus well understood from optical studies. Beyond $\langle n \rangle$ = 1, the plots of E_F vs $\langle n \rangle$ in Figure 2A all show similar asymptotic curvature, and notably, each curve plateaus at a similar potential near −1.37 V. Figure 2B plots the same E_F data vs average electron density ($\langle N \rangle$). Remarkably, all three curves are now superimposable within experimental uncertainty. E_F increases by <25 meV on going from $\langle N \rangle = 2 \times 10^{19}$ to 5×10^{19} cm^{-3}, which agrees well with previously reported values for electron−electron repulsion in ZnO nanocrystals with H^+ counterions.[31] Like $\langle N_{max} \rangle$, E_F^{max} is thus also independent of nanocrystal size for a given hole

DOI: 10.1021/jacs.5b06715
J. Am. Chem. Soc. 2015, 137, 11163−11169

quencher. For all three nanocrystal sizes, E_F maximizes near -1.37 V at $\langle N_{max}\rangle \approx (1.6 \pm 0.3) \times 10^{20}$ cm^{-3}. The data in Figure 2 provide a strong indication of Fermi-level pinning during nanocrystal photodoping. This result points to the conclusion that $\langle N_{max}\rangle$ in photodoped ZnO nanocrystals is determined specifically by the electron Fermi level, rather than by kinetic limitations.

It is important to note that all values of $\langle N\rangle$ and E_F reported here have been measured in the absence of ZnO UV photoexcitation. Under these conditions, and when rigorously anaerobic, $\langle N\rangle$ and E_F (or $\langle N_{max}\rangle$ and E_F^{max}) remain constant for very long times (e.g., k_{decay} < ~0.01/week at 298 K).[5] Kinetic contributions to $\langle N\rangle$ and E_F are observed under continuous UV photoexcitation, of course, where their precise steady-state (photostationary) values depend on the ZnO photoexcitation rate. Under illumination, steady-state values of $\langle N\rangle$ can exceed $\langle N_{max}\rangle$, and electron quasi-Fermi levels can exceed E_F^{max} (see Supporting Information). Upon termination of the UV illumination, however, $\langle N\rangle$ and E_F both relax quickly in the dark to $\langle N_{max}\rangle$ and E_F^{max}, at which point they are stable. Resuming the UV illumination again raises $\langle N\rangle$ and E_F to some steady-state values that depend on the UV irradiation parameters, but after terminating the UV illumination they again return to the same $\langle N_{max}\rangle$ and E_F^{max} (see Supporting Information). $\langle N_{max}\rangle$ and E_F^{max} are thus independent of the ZnO photoexcitation parameters. These observations strongly support the conclusion that $\langle N_{max}\rangle$ and E_F^{max} are determined thermodynamically, not kinetically.

We propose that the limit to E_F^{max} arises from the existence of a side redox reaction that occurs spontaneously at more reducing values of E_F. Specifically, we propose that E_F^{max} (and hence $\langle N_{max}\rangle$ and also $\langle n_{max}\rangle$) under the present photodoping reaction conditions is pinned by the reversibility of the EtOH oxidation reaction, i.e., by the spontaneous two-electron/two-proton transfer from heavily reduced ZnO nanocrystals to acetaldehyde. This back reaction should occur at the same potential regardless of the nanocrystal radius, consistent with the size-independent E_F^{max} observed in Figure 2. Experimentally, detection of EtOH formed from the proposed back reaction is not trivial, so to test the hypothesis of aldehyde hydrogenation by photoreduced ZnO nanocrystals, two sets of experiments were performed that indirectly probe the role of acetaldehyde. In the first, ZnO nanocrystals were photodoped to $\langle N_{max}\rangle$ in the presence of different amounts of added acetaldehyde. Figure 3 reveals that $\langle N_{max}\rangle$ decreases nearly linearly with added acetaldehyde, consistent with the hypothesized aldehyde hydrogenation chemistry.

In the second, benzaldehyde was used as a surrogate for acetaldehyde. In these experiments, ZnO nanocrystals were photodoped using EtOH as described above, but now in the presence of added benzaldehyde (see Supporting Information). Hydrogenation of benzaldehyde generates benzyl alcohol, which can be identified by its characteristic ^{1}H NMR peak at 4.2 ppm (vs TMS) arising from its α-CH_2 protons. ^{1}H NMR spectroscopy thus offers a convenient and sensitive probe of this chemistry. Figure 4A plots ^{1}H NMR data collected after various durations of UV illumination under the normal photodoping conditions, but now in the presence of added benzaldehyde. $\langle N_{max}\rangle$ is reached after ~45 min of UV excitation in these measurements (see Supporting Information), but over longer illumination times the formation of benzyl alcohol becomes evident from the appearance and growth of the broad α-CH_2 signal at 4.22 ppm, accompanied by a concomitant decrease in the intensity of the α-CH signal of benzaldehyde at 9.63 ppm. The broadening of the 4.2 ppm signal relative to that of neat benzyl alcohol (see Supporting Information) is likely due to association of the benzyl alcohol with the ZnO surface[32] or surface-capping ligands. Figure 4B plots integrated benzaldehyde and benzyl alcohol NMR intensities as a function of UV illumination time, showing that the changes in the concentrations of these two species are inversely correlated. Benzyl alcohol formation was confirmed by

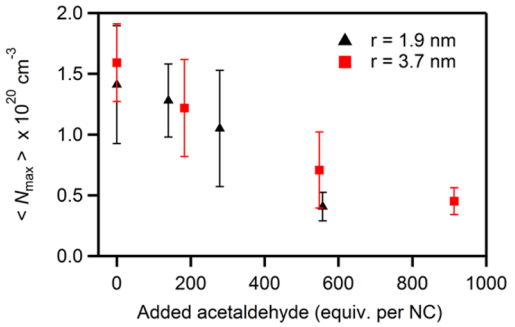

Figure 3. Maximum average electron densities ($\langle N_{max}\rangle$) achievable in colloidal ZnO nanocrystals photoreduced using EtOH as the hole scavenger, measured in the presence of added acetaldehyde. Data for r = 1.9 nm (5 μM, black triangles) and 3.7 nm (6 μM, red squares) ZnO nanocrystals are plotted. The error bars indicate $\pm\sigma$ from $\langle N\rangle$.

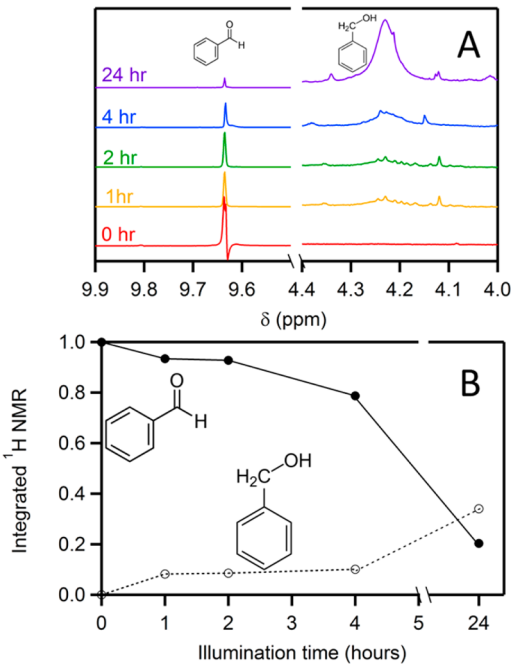

Figure 4. (A) ^{1}H NMR spectra (500 MHz) of TOPO-capped ZnO nanocrystals (r = 1.9 nm, 94 μM) in 1:3 toluene-d_8/benzene-d_6 spiked with EtOH and benzaldehyde in ~10^4× excess (per ZnO NC) at 0 h (red), 1 h (yellow), 2 h (green), 4 h (blue), and 24 h (violet) of UV illumination. Control measurements show no benzyl alcohol formation under UV irradiation in the absence of the ZnO nanocrystals (see Supporting Information). For clarity, the spectra are offset vertically and each side is normalized to the TOPO ligand signal at 2.5 ppm (not shown, see Supporting Information). (B) Integrated intensities of the α-CH benzaldehyde (9.8 ppm) and α-CH_2 benzyl alcohol (4.3 ppm) ^{1}H NMR signals relative to the TOPO CH_2 signal (2.5 ppm). These data are normalized to the benzaldehyde integrated intensity at 0 h. The presence of two α-CH_2 protons per benzyl alcohol was accounted for by halving the total normalized intensity for this signal. For reference, $\langle N_{max}\rangle$ is reached after ~45 min of UV excitation in these measurements.

DOI: 10.1021/jacs.5b06715
J. Am. Chem. Soc. 2015, 137, 11163−11169

GC-MS. Importantly, benzyl alcohol is not formed under the same conditions when benzaldehyde is irradiated by extensive UV illumination in the absence of the ZnO nanocrystals (see Supporting Information). We thus conclude that photoreduced ZnO nanocrystals can indeed hydrogenate aldehydes to form alcohols. Combined with the data from Figure 3, these results provide strong support for the conclusion that acetaldehyde hydrogenation is responsible for Fermi-level pinning during ZnO photodoping when using EtOH as the hole quencher, explaining at a microscopic level one of the more striking features of this nanocrystal redox chemistry.

Finally, we address the influence of charge-compensating cations on E_F. Charge-compensating cations play an integral role in the formation, stabilization, and reactivity of reduced ZnO nanocrystals.[6,16,31] In particular, protons greatly facilitate the reduction of ZnO NCs electrochemically[31] and by chemical reductants,[16] displaying exceptional effectiveness in stabilizing reduced ZnO nanocrystals relative to bulkier cations. To quantify the effects of protons, E_F values were measured for colloidal r = 1.9 nm ZnO nanocrystals reduced either photochemically (using EtOH) or chemically (using Cp^*_2Co). Figure 5 summarizes

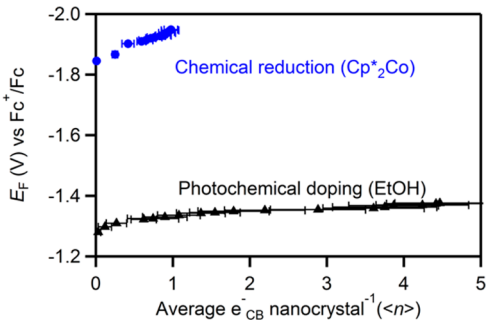

Figure 5. Comparison of E_F values measured for colloidal ZnO nanocrystals (r = 1.9 nm) reduced chemically using Cp^*_2Co (blue circles) and photochemically using EtOH (black triangles), both measured using the Cp_2Co^+/Cp_2Co couple as an optical redox indicator. The error bars indicate $\pm\sigma$ from the average value of $\langle n \rangle$.

these results. Strikingly, E_F is nearly 600 meV more negative for the chemically reduced nanocrystals than for the photodoped nanocrystals, and photodoping can introduce more than four times as many CB electrons as achieved by chemical reduction under these conditions. If E_F were determined solely by factors intrinsic to ZnO, such as the initial one-electron orbital energies or unscreened electron−electron repulsion, no difference in E_F would be observed with different reductants. The data in Figure 5 thus demonstrate and quantify the very large difference between CB electrons stabilized by H^+ and those stabilized by $Cp^*_2Co^+$.

DISCUSSION

Scheme 1 summarizes the changes in ZnO nanocrystal Fermi level during progressive photodoping using EtOH as the hole quencher and relates them to the changes observed upon chemical reduction by electron transfer from Cp^*_2Co. For the same nanocrystals reduced photochemically and chemically, comparison of E_F values measured at $\langle n \rangle$ = 1 (Figure 5) reveals that electrons compensated by H^+ are nearly 600 meV more stable than those compensated by $Cp^*_2Co^+$, a remarkably large difference. This difference could arise from more effective Coulombic stabilization (screening) of CB electrons by protons than by the bulky $Cp^*_2Co^+$ counterions, especially if protons are

Scheme 1

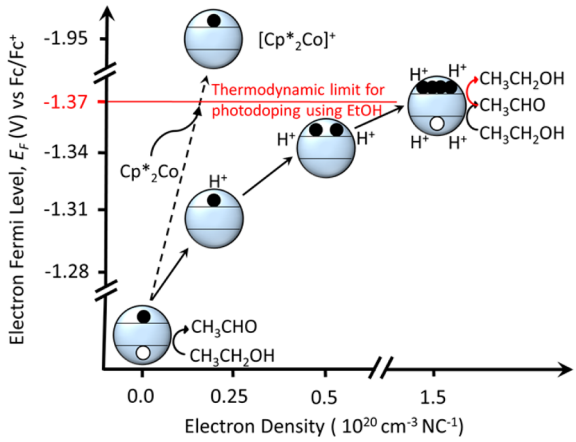

able to diffuse into the internal volumes of the nanocrystals, but it likely also reflects the formation of a strong O−H bond upon nanocrystal reduction using EtOH. Formation of a strong ZnO−H bond stabilizes the reduced nanocrystal product, lowers the electron's chemical potential, and in turn allows greater maximum electron densities to be attained in the same ZnO nanocrystals via photodoping than via reduction by Cp^*_2Co.

With extended photodoping (eq 1), E_F becomes dominated by electron−electron repulsive interactions that scale with electron density, yielding a single relationship between E_F and $\langle N \rangle$ that holds for all nanocrystal sizes. Between $\langle N \rangle = 2 \times 10^{19}$ and 5×10^{19} cm^{-3}, E_F rises with a slope of ca. −130 meV/(10^{20} cm^{-3}), but subsequently shows asymptotic behavior indicative of Fermi-level pinning. The microscopic origin of the Fermi-level pinning has been identified as the acetaldehyde hydrogenation reaction, which at low electron densities is negligible but becomes more favorable as E_F increases. When E_F reaches ca. −1.37 V vs Fc^+/Fc (E_F^{max}), at $\langle N_{max} \rangle \approx 1.6 \times 10^{20}$ cm^{-3}, UV illumination yields no further stable electron accumulation within the ZnO nanocrystals. At this point, further EtOH photooxidation is followed by spontaneous (dark) aldehyde hydrogenation (eq 3). The E_F^{max} values reported here are thus dictated by the dark reverse reaction of eq 1.

$$e^-_{CB}:ZnO{-}H^+ + 1/2CH_3CHO \rightarrow ZnO + 1/2CH_3CH_2OH \quad (3)$$

It is possible that this reaction continues on an imperceptibly slow time scale (>days) after its apparent equilibration within seconds or minutes. Strictly speaking, these photodoped nanocrystals would then be kinetically stable but not truly at equilibrium. This scenario could arise from proton diffusion. For example, it is possible that the correct proton configurations at the nanocrystal surfaces do not exist in these reduced nanocrystals because of proton diffusion into the internal nanocrystal volumes, driven by the greater electron density within the nanocrystal cores and by proton−proton repulsion in the types of structures with two proximal protons that might be required for aldehyde hydrogenation. At this time, the details of this reaction remain poorly understood. Clarification of such details will be the focus of future studies with this system.

Heterogeneous catalytic hydrogenation of aldehydes by ZnO has been reported previously, but the reaction generally takes place at elevated temperature (~650 K) under continuous H_2 flow,[32,33] or requires a noble metal co-catalyst,[34] and it is not driven by photons. Here, aldehyde hydrogenation occurs as the

DOI: 10.1021/jacs.5b06715
J. Am. Chem. Soc. 2015, 137, 11163−11169

result of a very negative E_F in ZnO achieved by extensive nanocrystal photoreduction. Although further analysis of this aldehyde hydrogenation reactivity is beyond the scope of the present study, this observation of multi-electron/multi-proton chemistry involving heavily reduced semiconductor nanocrystals generated photochemically could have interesting implications in the area of solar fuels.[35,36]

Finally, recent work has demonstrated analogous photodoping of colloidal In_2O_3 nanocrystals using EtOH as the hole quencher,[7] as well as photodoping of ZnO[6] and CdE (E = S, Se, Te)[8] nanocrystals with a variety of hydride hole quenchers (e.g., Li[Et_3BH]). Although beyond the scope of the present study, it is interesting to consider the possibility that Fermi-level pinning might also be responsible for the maximum photodoping levels observed in these nanocrystals. In_2O_3 is most similar to ZnO. In_2O_3 nanocrystals can be photodoped using EtOH to comparable maximum electron densities as in ZnO nanocrystals, which would be consistent with a similar limiting mechanism, but the different surface chemistries of In_2O_3 and ZnO nanocrystals can reasonably be anticipated to lead to different hydrogenation catalysis and hence different limiting Fermi levels. In contrast with ZnO nanocrystals, CdE nanocrystals often have mid-gap surface electron traps that may impact photodoping, and these nanocrystals also do not form strong bonds with protons, suggesting unrelated redox chemistries may instead dominate. Overall, while the specific redox processes described here for ZnO may not be central in these other photodoping chemistries, the concept of photodoping limited by competing redox reactions rather than by photophysical recombination kinetics may be general. Future studies on photodoping involving these other materials will address these interesting open questions.

CONCLUSION

A simple optical method employing a solvated redox indicator has been applied for *in situ* determination of reduced ZnO nanocrystal redox potentials. These measurements reveal that the Fermi levels of solutions of nanocrystals possessing an average of just one CB electron per nanocrystal can vary by over 600 meV depending upon the method of charge compensation, and also reveal electron quantum-confinement effects for a fixed charge-compensating cation (H^+) but different nanocrystal sizes. For ZnO nanocrystals photodoped using EtOH as the hole quencher, the Fermi level becomes independent of nanocrystal size at average electron densities of $\sim 2 \times 10^{19}$ cm^{-3}. The maximum carrier densities achievable via photodoping, $\sim 1.6 \times 10^{20}$ cm^{-3}, are found to be determined by electron Fermi-level pinning. Microscopically, this Fermi-level pinning is identified as arising from the spontaneous two-electron/two-proton hydrogenation of acetaldehyde, which reverses the EtOH photooxidation reaction. This hydrogenation reaction, and hence the maximum nanocrystal photodoping level, occurs at the same potential for all nanocrystal sizes, explaining the microscopic basis for the maximum electron densities achievable via this photochemistry.

ASSOCIATED CONTENT

Supporting Information

The Supporting Information is available free of charge on the ACS Publications website at DOI: 10.1021/jacs.5b06715.

Additional experimental results (10 figures) (PDF)

AUTHOR INFORMATION

Corresponding Author

*gamelin@chem.washington.edu

Notes

The authors declare no competing financial interest.

ACKNOWLEDGMENTS

This research was supported financially by the U.S. National Science Foundation (CHE-1151726 and CHE-1506014 to D.R.G., Graduate Research Fellowship DGE-1256082 to A.M.S.), the U.S. National Institutes of Health (Postdoctoral Fellowship F32GM110876 to E.Y.T.), and the University of Washington Clean Energy Institute. The authors gratefully acknowledge Prof. James Mayer for fruitful discussions.

REFERENCES

(1) Haase, M.; Weller, H.; Henglein, A. *J. Phys. Chem.* **1988**, *92*, 482−487.
(2) Shim, M.; Guyot-Sionnest, P. *J. Am. Chem. Soc.* **2001**, *123*, 11651−11654.
(3) Wood, A.; Giersig, M.; Mulvaney, P. *J. Phys. Chem. B* **2001**, *105*, 8810−8815.
(4) Germeau, A.; Roest, A. L.; Vanmaekelbergh, D.; Allan, G.; Delerue, C.; Meulenkamp, E. A. *Phys. Rev. Lett.* **2003**, *90*, 097401.
(5) Liu, W. K.; Whitaker, K. M.; Kittilstved, K. R.; Gamelin, D. R. *J. Am. Chem. Soc.* **2006**, *128*, 3910−3911.
(6) Schimpf, A. M.; Gunthardt, C. E.; Rinehart, J. D.; Mayer, J. M.; Gamelin, D. R. *J. Am. Chem. Soc.* **2013**, *135*, 16569−16577.
(7) Schimpf, A. M.; Lounis, S. D.; Runnerstrom, E. L.; Milliron, D. J.; Gamelin, D. R. *J. Am. Chem. Soc.* **2015**, *137*, 518−524.
(8) Rinehart, J. D.; Schimpf, A. M.; Weaver, A. L.; Cohn, A. W.; Gamelin, D. R. *J. Am. Chem. Soc.* **2013**, *135*, 18782−18785.
(9) Cohn, A. W.; Janßen, N.; Mayer, J. M.; Gamelin, D. R. *J. Phys. Chem. C* **2012**, *116*, 20633−20642.
(10) Markham, M. C.; Hannan, M. C.; Paternostro, R. M.; Rose, C. B. *J. Am. Chem. Soc.* **1958**, *80*, 5394−5397.
(11) Cunningham, J.; Hodnett, B. K. *J. Chem. Soc., Faraday Trans. 1* **1981**, *77*, 2777−2801.
(12) van Dijken, A.; Meulenkamp, E. A.; Vanmaekelbergh, D.; Meijerink, A. *J. Lumin.* **2000**, *90*, 123−128.
(13) Wood, A.; Giersig, M.; Hilgendorff, M.; Vilas-Campos, A.; Liz-Marzán, L. M.; Mulvaney, P. *Aust. J. Chem.* **2003**, *56*, 1051−1057.
(14) Hayoun, R.; Whitaker, K. M.; Gamelin, D. R.; Mayer, J. M. *J. Am. Chem. Soc.* **2011**, *133*, 4228−4231.
(15) Cohn, A. W.; Kittilstved, K. R.; Gamelin, D. R. *J. Am. Chem. Soc.* **2012**, *134*, 7937−7943.
(16) Valdez, C. N.; Braten, M.; Soria, A.; Gamelin, D. R.; Mayer, J. M. *J. Am. Chem. Soc.* **2013**, *135*, 8492−8495.
(17) Schwartz, D. A.; Norberg, N. S.; Nguyen, Q. P.; Parker, J. M.; Gamelin, D. R. *J. Am. Chem. Soc.* **2003**, *125*, 13205−13218.
(18) Norberg, N. S.; Gamelin, D. R. *J. Phys. Chem. B* **2005**, *109*, 20810−20816.
(19) Meulenkamp, E. A. *J. Phys. Chem. B* **1998**, *102*, 5566−5572.
(20) Schimpf, A. M.; Ochsenbein, S. T.; Buonsanti, R.; Milliron, D. J.; Gamelin, D. R. *Chem. Commun.* **2012**, *48*, 9352−9354.
(21) Schrauben, J. N.; Hayoun, R.; Valdez, C. N.; Braten, M.; Fridley, L.; Mayer, J. M. *Science* **2012**, *336*, 1298−1301.
(22) Gordon, K. R.; Warren, K. D. *Inorg. Chem.* **1978**, *17*, 987−994.
(23) Liu, W. K.; Whitaker, K. M.; Smith, A. L.; Kittilstved, K. R.; Robinson, B. H.; Gamelin, D. R. *Phys. Rev. Lett.* **2007**, *98*, 186804.
(24) Schimpf, A. M.; Thakkar, N.; Gunthardt, C. E.; Masiello, D. J.; Gamelin, D. R. *ACS Nano* **2014**, *8*, 1065−1072.
(25) Shim, M.; Guyot-Sionnest, P. *Nature* **2000**, *407*, 981−983.
(26) Goings, J. J.; Schimpf, A. M.; May, J. W.; Johns, R. W.; Gamelin, D. R.; Li, X. *J. Phys. Chem. C* **2014**, *118*, 26584−26590.
(27) Reiss, H. *J. Phys. Chem.* **1985**, *89*, 3783−3791.

DOI: 10.1021/jacs.5b06715
J. Am. Chem. Soc. 2015, 137, 11163−11169

(28) Khan, S. U. M.; Kainthla, R. C.; Bockris, J. O. M. *J. Phys. Chem.* **1987**, *91*, 5974−5977.
(29) Roest, A. L.; Kelly, J. J.; Vanmaekelbergh, D.; Meulenkamp, E. A. *Phys. Rev. Lett.* **2002**, *89*, 036801.
(30) Connelly, N. G.; Geiger, W. E. *Chem. Rev.* **1996**, *96*, 877−910.
(31) Roest, A. L.; Germeau, A.; Kelly, J. J.; Vanmaekelbergh, D.; Allan, G.; Meulenkamp, E. A. *ChemPhysChem* **2003**, *4*, 959−966.
(32) Haffad, D.; Kameswari, U.; Bettahar, M. M.; Chambellan, A.; Lavalley, J. C. *J. Catal.* **1997**, *172*, 85−92.
(33) Bowker, M.; Houghton, H.; Waugh, K. C. *J. Chem. Soc., Faraday Trans. 1* **1982**, *78*, 2573−2582.
(34) Mäki-Arvela, P.; Hájek, J.; Salmi, T.; Murzin, D. Y. *Appl. Catal., A* **2005**, *292*, 1−49.
(35) Smestad, G. P.; Steinfeld, A. *Ind. Eng. Chem. Res.* **2012**, *51*, 11828−11840.
(36) Rausch, B.; Symes, M. D.; Chisholm, G.; Cronin, L. *Science* **2014**, *345*, 1326−1330.

DOI: 10.1021/jacs.5b06715
J. Am. Chem. Soc. 2015, 137, 11163−11169